Deformation Behavior in a Neutron Irradiated Generation II FeCrAl Alloy for Accident Tolerant Fuel Cladding

**Nuclear Technology
Research and Development**

*Prepared for
U.S. Department of Energy
Advanced Fuels Campaign
K.G. Field, D. Zhang, M.N. Gussev,
K. Smith, & K.C. Littrell
Oak Ridge National Laboratory
September 22nd, 2017*

SUMMARY

Preliminary work has been completed to evaluate the deformation behavior of the Generation II FeCrAl alloy class. The Generation II alloy, C35M, was neutron irradiated within the High Flux Isotope Reactor followed by post-irradiation examination to evaluate the mechanical properties, irradiated microstructure, deformation modes, and deformation microstructure. Complementary characterization techniques were used in this evaluation. It was found that after irradiation to 1.8 dpa at 364°C that the C35M specimen failed in a ductile manner. The observed deformation microstructure showed a high density of line dislocations, dislocation networks, and dislocation pile-ups. The observed performance and structures are consistent with literature studies on high-Cr FeCr alloys that were thermally aged at 500°C. The observed results suggest that Generation II FeCrAl alloys retain ductility under low-dose, prototypical LWR irradiation conditions.

CONTENTS

FIGURES

TABLES

ACRONYMS

ADF	Annular Dark Field
ALARA	As Low as Reasonably Achievable
ATF	Accident Tolerant Fuel
BF	Bright Field
DOE	Department of Energy
EFTEM	Energy Filtered Transmission Electron Microscopy
FIB	Focused Ion Beam
HFIR	High Flux Isotope Reactor
IMET	Irradiated Materials Examination and Testing
LAMDA	Low Activation Materials Development and Analysis
LWR	Light Water Reactor
NEET	Nuclear Energy Enabling Technologies
ORNL	Oak Ridge National Laboratory
SANS	Small Angle Neutron Scattering
SEM	Scanning Electron Microscopy
STEM	Scanning Transmission Electron Microscopy
TE	Total Elongation
UE	Uniform Elongation
US	United States
UTS	Ultimate Tensile Strength
YS	Yield Strength

DEFORMATION BEHAVIOR IN NEUTRON IRRADIATED GENERATION II FECRAL ALLOYS FOR ACCIDENT TOLERANT FUEL CLADDING

1. INTRODUCTION

The United States (US)-based light water reactor (LWR) fleet has experienced a long history of safe operation. The current fleets LWR fuel system is composed of UO_2 fuel and zirconium (Zr)-based alloy claddings. Given the safe operation within the US, the nuclear accident that occurred in Japan in 2011 has revealed the susceptibility of the current UO_2-Zr fuel system to accident scenarios. Recently, both domestic and international research programs have been put in place to explore advanced nuclear fuel cladding concepts that improve on the accident tolerance of LWRs. A primary characteristic of these concepts is improved high temperature steam oxidation resistance during accident scenarios compared to the current Zr-based cladding options [1]. Iron-chromium-aluminum (FeCrAl) alloys are an attractive advanced cladding option as these alloys have been demonstrated to form protective alumina under high-temperature steam oxidation resulting in significant (10-100×) reductions in the parabolic oxidation rate of the cladding [1–3].

Previous work on deformation behavior of FeCrAl alloys as accident tolerant fuel (ATF) concepts within the US domestic research program has focused on model alloy systems [4,5]. These studies showed that the deformation behavior in FeCrAl alloys can, in-part, be linked to the evolution of the radiation-induced/enhanced microstructure. This concept was primarily developed using a dispersed barrier hardening model. Given this work, little has been completed to determine the deformation mechanics and deformed microstructure to illicit how these microstructural features promote either ductile or brittle fracture in neutron irradiated FeCrAl alloys. Promotion of ductile fractures is the key to the acceptable performance of FeCrAl cladding under normal operation.

Previous works by Park et al. [6] and Triki et al. [7] on aged high-Cr ferritic alloys has shown that a transition in the deformation mode from deformation bands to twinning occurs in this material class and that transition can speculatively be linked to the increased precipitation of the Cr-rich α' in long-term aged FeCr alloys. Figure 1 provides a notional deformation map for FeCr alloys based on the studies of Triki et al. and Park et al. Severe embrittlement has been linked to the presence of twinning within the deformed microstructure. Similar behavior has been shown for irradiated FeCr alloys [8], but to date has not been extensively investigated for FeCrAl alloys.

Here, preliminary work has sought to determine the deformation behavior within the FeCrAl alloys class. Specifically, the Oak Ridge National Laboratory (ORNL)-developed Generation II [9] FeCrAl alloys are of interest as they are actively being pursued for deployment within a commercial LWR within calendar year 2018. The alloy selected was C35M which is a 13 wt.% Cr, 5 wt.% Al FeCrAl alloy that has been extensively characterized within previous programs. The C35M alloy was irradiated as sheet tensile specimens within the High Flux Isotope Reactor (HFIR) at ORNL followed by extensive post-irradiation examination (PIE). Tensile tests of sub-sized and ultra-miniature sized tensile specimens combined with post-test fractography were used to determine the mechanical performance including values for yield stress, ultimate tensile stress, total elongation, and uniform elongation. Advanced characterization, including scanning transmission electron microscopy (STEM) and small angle neutron scattering (SANS), was used to evaluate the irradiated microstructure. Finally, site-specific sample preparation using a focused ion beam (FIB) on the fractured specimens was completed to observe the deformed microstructure and determine what deformation mode regime and deformation microstructure regime the C35M alloy resides within after irradiation to low-dose, nominal LWR conditions.
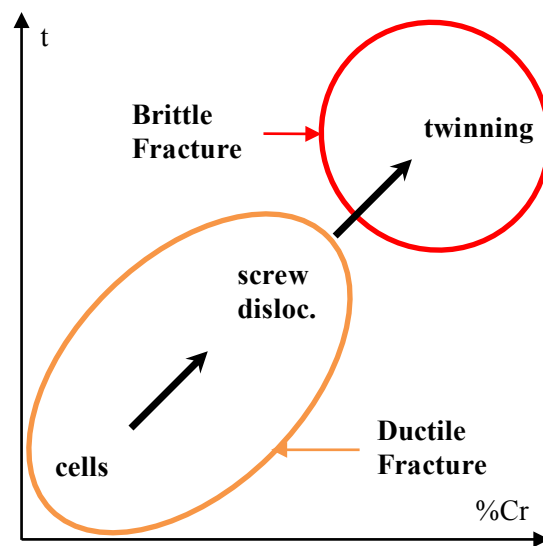
Figure 1: Qualitative schematic of deformation microstructures and deformation mechanisms as a function of Cr concentration and aging time for high-Cr ferritic steels. Aging performed at or below 500°C. Adapted from Ref. [7] and supplemented with information in Ref. [6].

2.   MATERIALS AND METHODS

2.1   Selected materials

The selected alloy was a Generation II ORNL-developed FeCrAl alloy, C35M. C35M is a 13.06 wt.% Cr, 5.13 wt.% Al, 0.01 wt.% Y, 0.18 wt.% Si, and 1.96 wt.% Mo alloy with nominal grain sizes of 1-5 μm [9]. This alloy was selected as no neutron irradiated C26M alloy, the leading candidate for deployment as cladding in a commercial LWR, was available for the study. C35M provides a reasonable balance between the Cr and Al content with a known ability to produce the Cr-rich α' phase. The higher Cr and lower Al content in C35M compared to C26M means the observed effects are conservative based on suspected α' hardening effects.

The heat used within this work was produced at a commercial vendor using vacuum induction melting to produce 18 kg ingots in the form of 81 mm × 300 mm cylinders. The ingots were homogenized at 1200°C in Ar for 4h followed by hot forging at 800°C with 50% total thickness reduction. An additional 40% reduction was completed at 800°C using hot rolling techniques. Hot rolling was followed with an 800°C anneal for 1 h in air. Final thickness reductions were completed using warm-rolling at 300°C with a total thickness reduction of 80-90%. A final anneal was completed at 650°C for 1 hr in air. The resulting grain structure was elongated grains in the rolling direction with the formation of deformed sub-grains.

The C35M feedstock was machined into irradiation tensile specimens using electric discharge machining. For SANS and baseline mechanical testing analysis, the SS-J2 specimen was used. The SS-2E test specimens irradiated and mechanically tested as reference specimens under the Department of Energy (DOE) Nuclear Energy Enabling Technologies (NEET) Reactor Materials program was used for targeted STEM-based imaging. This specimen geometry was developed and proven in the NEET program to provide representative mechanical performance data to the SS-J2 geometry but significantly reduces the sample volume [10]. This sample reduction means full tensile specimens can be shipped and investigated in the Low Activation Materials Development and Analysis (LAMDA) laboratory while adhering to DOE

principles of as low as reasonably achievable (ALARA), all while not sacrificing the integrity of this scientific study. Both specimens were irradiated in the same FCAT irradiation series capsule.

2.2 Irradiation testing

SS-J2 and SS-2E tensile specimens were irradiated within the FCAT irradiation series to nominal damage dose of 2 dpa at a target temperature of 330°C. Additional capsules were irradiated to varying doses and temperatures, but here the focus is on the FCAT02 capsule irradiated to the specified conditions. The FCAT02 irradiation capsule was irradiated in the central flux trap of the High Flux Isotope Reactor (HFIR). The capsule contained a series of tensile test specimens and passive SiC thermometry specimens. FCAT02 was dismantled after irradiation in the Irradiated Materials Examination and Testing (IMET) facility. No post-irradiation sample preparation was completed on the tensile specimens prior to mechanical testing.

The SiC thermometry specimens were analyzed using dilatometric analysis after irradiation to determine the average irradiation temperature of the FCAT02 capsule. Dilatometry was competed up to a maximum temperature of 600°C at a constant ramp rate of 1°C/min and a cooling rate of 2.5°C/ min using a Netzsch 402 CD dilatometer. Two samples from each axial position (top, middle, and bottom) were tested and temperatures determined using the algorithms developed by Campbell et al. [11]. The resulting provided a mean capsule irradiation temperature of 363.6 ± 23.1°C. The final irradiation dose was estimated as 1.8 dpa with a dose rate of 9.3×10^{-7} dpa/s based on the axial position within the central flux trap and the run time of Cycle 465 in HFIR (24.6 days).

2.3 Mechanical testing

Tensile testing of the SS-J2 specimen (ID: MF04) was completed using a Instron universal testing machine remotely controlled within the IMET hot cell facility. The relative volume of the SS-J2 specimen and irradiation conditions resulted in residual radioactivity (>>100 mrem/hr at 30 cm) that necessitated the shielding facilities within IMET. The SS-J2 specimen was shoulder loaded at a nominal strain rate of 10^{-3} s^{-1} in laboratory air at room temperature. Engineering stress-strain curves were developed based on the pre-irradiation dimensional inspection data and the digitally recorded crosshead displacements. Although multiple C35M specimens were irradiated in FCAT02, only one specimen was tested. Fractography was completed using a 5 kV beam at a working distance of 10 mm on a JEOL JSM-6010A scanning electron microscope (SEM). Testing of the SS-2E specimen (ID: F04) was completed under the respective NEET Reactor Materials program; details can be found in reports of this program [12,13]. The mechanical testing configuration was designed specifically to mimic the properties found using the IMET hot cell facility.

2.4 Small angle neutron scattering

SANS was performed to non-destructively assess the extent of α' precipitation in the irradiated C35M specimen. SANS analysis has been shown to provide similar results to atom probe tomography [14]. SANS was performed on one-half of the broken SS-J2 tensile specimen on the HFIR General Purpose SANS [29] beam line. The latent sample radioactivity of the broken tensile necessitated specialized designs to acquire accurate SANS signals while reducing the radiological threat of the specimen. Here, a specialized lead sample container was developed to shield the specimen during SANS investigations. High purity lead is transparent to the analyzing neutron beam thus shielding the specimen while

simultaneously allowing for SANS measurements to be performed. Figure 2 shows one of these containers prior to and after non-irradiated sample loading.
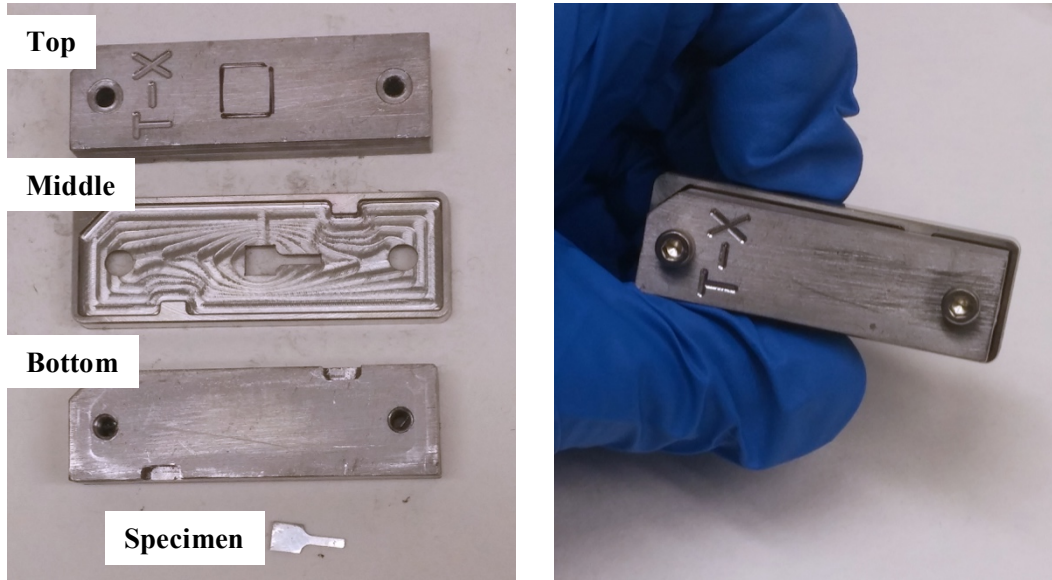
Figure 2: Photographs showing the specimen high-purity lead encapsulation prior to SANS analysis.

SANS measurements were made at room temperature under a saturating magnetic field H ($\cong$1 T), to allow for the separation of the magnetic and nuclear scattering cross-sections. Scattering intensities (*I(q)*) were modeled assuming that the α' precipitates are considered monodispersed spheres within the α matrix and exhibit a hard-sphere potential. Previous SANS analysis [4,14] shows the low-q region of the scattering curves can be estimated using a low-q inverse power law. The result is the two models can be completed in summation resulting in the I(q) taking the functional form*:

$$I(q) = V\eta^{\alpha'}\Delta\rho^2 P(q,r)S(q,R_{hs},\eta) + (Aq^{-m} + B) , \tag{1}$$

where V is the volume of the precipitates; $\eta^{\alpha'}$ is the volume fraction of α' precipitates; $P(q,r)$ is the particle form factor for spherical precipitates [32]; $S(q,R_{hs},\eta)$ is the hard-sphere structure factor [30]; and $Aq^{-m} + B$ is the inverse power law, where A is the power law length scale factor, m is the power law exponent, and B is the residual background in the measurements. The scattering contrast, $\Delta\rho^2$, is given by $\Delta\rho^2 = \Delta\rho_{nucl}^2 + \Delta\rho_{mag}^2$ when the intensity is taken perpendicular to the magnetic field and $\Delta\rho^2 = \Delta\rho_{nucl}^2$ when the intensity is taken parallel to the magnetic field. In both cases, Eqn. 1 was fitted to the experimental data using a modified Levenberg-Marquardt algorithm. Precipitate volume fraction, number density, and radius of the α' precipitates was extracted using the method described by Pedersen [30].

The anisotropy in scattering intensity allows for determination of the nominal chemical composition of the Cr-rich α' phase and the Fe-rich α phase by method of determining the 'A-ratio.' The A ratio depends on the chemical composition, magnetization and atomic density variations between the precipitates and the matrix and is given by:

$$A = \frac{I(q)_{\perp H}}{I(q)_{\parallel H}} = \frac{\Delta\rho_{mag}^2 + \Delta\rho_{nucl}^2}{\Delta\rho_{nucl}^2} = 1 + \frac{\Delta\rho_{mag}^2}{\Delta\rho_{nucl}^2} \tag{1}$$

The A-ratio for the α' phase in the α-matrix is routinely quoted at values of 2.03-2.18 [15–18] with the value varying depending on the composition and assumed magnetism of the precipitates [19]. Other common microstructural features for ferritic alloys including Cr-rich carbides and vacancy clusters have values of >3 and 1.37-1.4, respectively.

2.5   Targeted STEM-based imaging

Specimens for STEM were prepared from specific sites of interest using standard FIB lift-out procedures. A FEI Quanta 3D 200i DualBeam FIB or FEI Versa 3D DualBeam FIB was used to create the cross-sectional FIB lift-out specimens. Two different locations of interest were prepared, one being very near the fracture surface where the resulting grains saw high local strain and one further away from the fracture surface where the local strain was of lower value. The general locations are shown schematically in Figure 3. Additional specimens were extracted from the tensile head region of the specimen to provide the non-deformed microstructure. Previous characterization of the local strains in the tensile heads of SS-2E specimens indicates that the tensile head is generally free of deformation [10]. Care was taken during specimen thinning to minimize specimen twisting and bending. Specimens were thinned to electron transparency followed by low-angle, low-keV ion polishing to reduce artifacts from the FIB sample preparation.
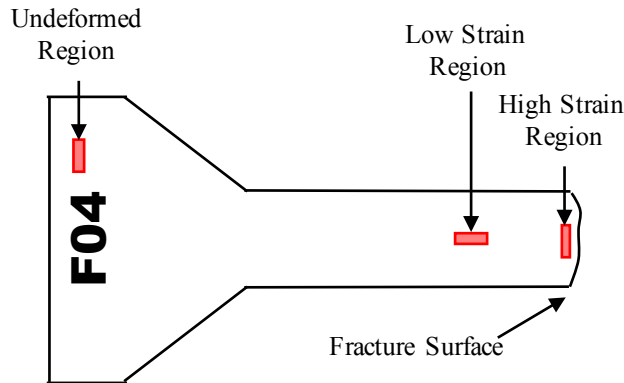
Figure 3: Schematic showing location of FIB-produced for STEM-based imaging.

FIB specimens from the non-deformed region, low strain region, and high strain region were characterized using a JEOL JEM-2100F field emission gun STEM operating at 200 kV. Specimen thicknesses for number density measurements were determined using energy filtered transmission electron microscopy (EFTEM) on the same microscope. Dislocation structures were examined using on-[100] zone axis STEM operating in simultaneous bright field (BF) and annular dark field (ADF) modes. Orientating the specimens to the [100] zone axis allows for imaging of $a/2\langle111\rangle$ dislocation loops as open ellipses, whereas $a\langle100\rangle$ dislocation loops are either edge-on or in-plane; the result is stark line contrast or diffuse contrast of circular/faceted loops, respectively [20]. Line dislocations including dislocation cells and networks can be imaged in a similar manner.

3.   RESULTS

3.1   Unirradiated microstructures

The as-received microstructure of C35M was characterized to be fully ferritic with a combination of recrystallized grains and chains of smaller deformed (non-recrystallized) grains as shown in Figure 4. This microstructure is consistent with the warm-rolled conditions of the alloy feedstock. The recrystallized grains generally showed a low dislocation density with limited networking or cell structures. Due to the low density within the recrystallized grains, an accurate estimation of the dislocation density could not be determined (i.e. too low to be statistically significant). The smaller, deformed grains showed a higher density of line dislocations which presented themselves as tangles and networks within the grains. Grain sizes ranged on the size of ~1-5 μm.

(a)

10 μm

(b)

1 μm
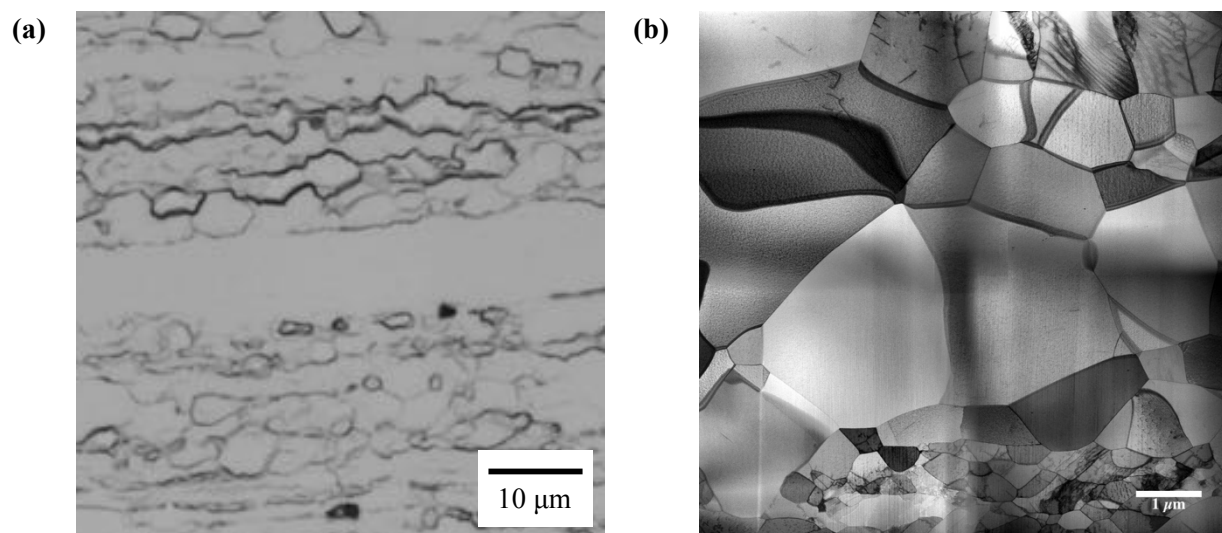
Figure 4: Grain structure of C35M revealed using optical microscopy (a) and STEM (b). Multiple images stitched in (b) to produce a large field of view.

3.2   Irradiated and non-deformed microstructures

The dislocation loop and dislocation line structure of the C35M alloy after neutron irradiated is shown in Figure 5. The presence of different dislocation loop types were determined via their morphology and using the dislocation loop maps provided by Yao et al. [20]. Figure 5 shows dislocation loop morphologies consistent with those expected of dislocation loops with Burgers vectors of both $a/2 \langle 111 \rangle$ (open ellipses) and $a\langle 100 \rangle$ (stark, straight, edge-on line segments and faint faceted circles). Preliminary quantitative loop counting estimated $a/2 \langle 111 \rangle$ loop density as $1.6 \times 10^{21} \pm 1.0 \times 10^{20}$ m^{-3} with an average diameter of 22.9 ± 3.0 nm while the $a\langle 100 \rangle$ loops had a density of $1.1 \times 10^{21} \pm 8.2 \times 10^{19}$ m^{-3} and an average diameter of 15.2 ± 9.9 nm. Limited dislocation networking was observed in the larger recrystallized grains that were characterized. The line dislocation density was estimated at $8.4 \times 10^{13} \pm 5.1 \times 10^{12}$ m^{-2}. Many of the "half-moon" or curved line dislocations observed in Figure 5 are the result of $a/2 \langle 111 \rangle$ dislocation loops being truncated by the free surface(s) of the STEM lamellae. Small ($\lesssim 10$ nm) dislocation loops which could not be distinctively characterized based on morphology were classified as black dots. The black dot number density was estimated at $5.2 \times 10^{21} \pm 2.6 \times 10^{20}$ m^{-3} with an

average diameter of 8.6 ± 2.6 nm. No evidence of void or bubble formation indicative of swelling was observed in the irradiated specimens.
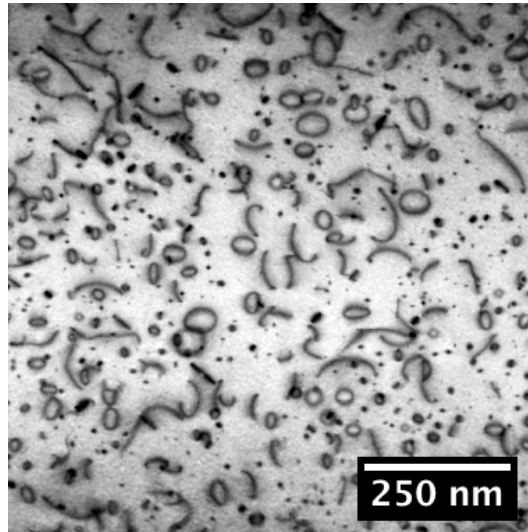
Figure 5: Non-deformed defect structure in neutron irradiated C35M (1.8 dpa at 364°C). Imaged using on-[100] zone axis STEM bright field imaging.

The Cr-rich α' phase was not observed using STEM-based techniques. SANS was conducted to detect and quantify the presence of α' within the non-deformed head of the SS-J2 tensile specimen. Figure 6 shows the scattering intensity plots for the unirradiated and irradiated specimen of C35M. The "hump" observed for the irradiated specimen is indicative of the Cr-rich α' phase within the material. Application of a model based on a spherical exclusion volume determined the number density of the α' phase to be $1.8 \times 10^{24} \pm 2.6 \times 10^{23}$ m^{-3} with an average diameter of 3.6 ± 0.1 nm and volume fraction of 4.5 ± 0.6 %. The A-ratio was determined to be 1.87 which is lower than those quoted for α' within the literature but those determinations are based on assuming non-magnetic, highly Cr-enriched spherical precipitates. Previous studies have shown that α' in neutron irradiated FeCrAl does not reach the observed saturation values of >80 wt.% within the dose and temperature regime studied. Inclusion of significant amounts of Fe into the α' phase could result in varied A-ratio values and hence here it is concluded the scattering observed in Figure 6 is indeed due to the Cr-rich α' phase.
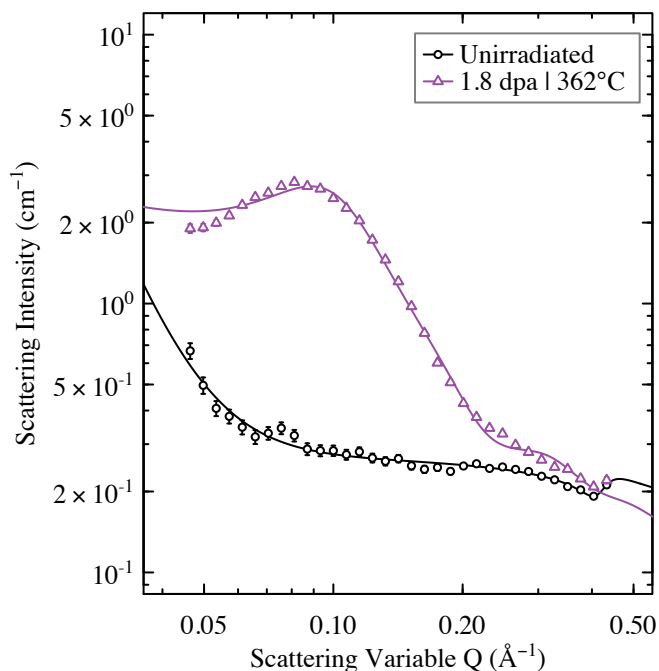
Figure 6: Experimental scattering intensities (symbols) and best-fit model (lines) of neutron-irradiated C35M.

3.3 Mechanical properties

The mechanical properties of both the SS-J2 neutron irradiated C35M specimen and the SS-2E specimen have been reported in previous reports of this program and the NEET reactor materials program [21,22]. For detailed observations on the mechanical properties including localized strain assessments the reader is referred to the cited reports. In general, the C35M alloy showed radiation-induced hardening with an increase in the yield strength and reduction of ductility. After irradiation, no load carrying capacity after the initial yield was observed. The mechanical properties derived from the engineering stress-strain curves are presented in Table 1.

Table 1: Mechanical properties of C35M before and after neutron irradiation to 1.8 dpa at 364°C.

Condition	Specimen Geometry	Specimen ID	YS (MPa)	UTS (MPa)	UE (%)	TE (%)	Fracture Type
Unirradiated	SS-J2	MF29	631	719	11.6	19.5	Ductile
Irr.: 1.8 dpa at 364°C	SS-J2	MF04	903	944	4.2	11.5	Ductile
Irr.: 1.8 dpa at 364°C	SS-2E	F04	914	937	2.7	10.4	Ductile

*YS: Yield Strength, UTS: Ultimate tensile strength, UE: Uniform elongation, TE: total elongation

The fracture surface of the neutron irradiated SS-J2 specimen observed via SEM is shown in Figure 7. The specimen showed significant reduction of area indicating a reasonable degree of deformability at room temperature after irradiation. The fracture was characterized to have a dimple-cone morphology indicative of a ductile fracture. Local necking can be observed in the planar observation of the specimen. High magnification images show the presence of dislocation channels on the surface but with a complex morphology compared to those typically seen in face-centered-cubic irradiated materials. The density of channels decreased as the distance from the fracture surface increased.

(a)   **(b)**
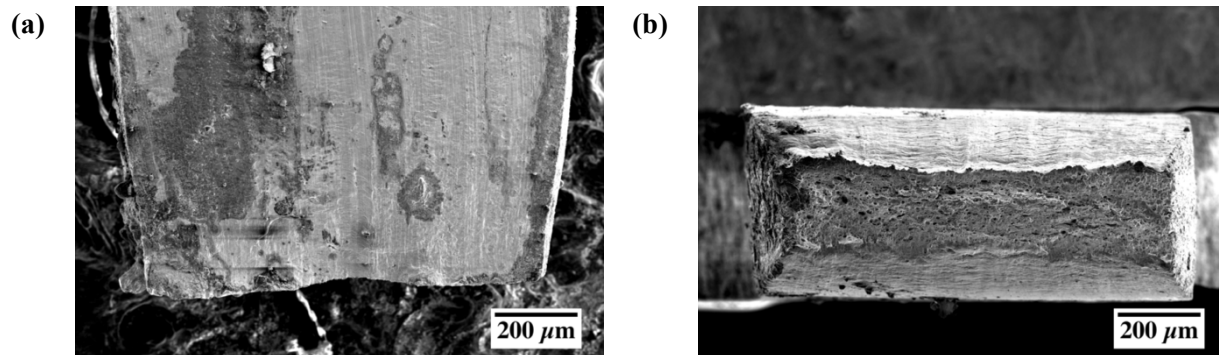
Figure 7: SEM micrographs showing the fracture surfaces of C35M irradiated to 1.8 dpa at 364°C (ID: MF04) after tensile testing at room temperature; (a) planar view and (b) top-down view.

3.4   Irradiated and deformed microstructures

Figure 8 shows the local dislocation structure associated with both the low strain and high strain areas after deformation. Within the low strain area, the presence of dislocation loops and irradiated microstructures are still observed. A large density of line dislocations is also observed. The observation of dislocation loops within the structure would suggest that at lower strains that glissile line dislocations have not completely eliminated the irradiated microstructure and that the dislocation loops and Cr-rich α' are still active barriers to dislocation motion. Within the high strain area, the irradiated microstructure is completely destroyed and only a high density of network dislocations aggregated into a local cell structure is observed. Both regions showed no presence of dislocation channeling or twinning but did show dislocation pile-ups.
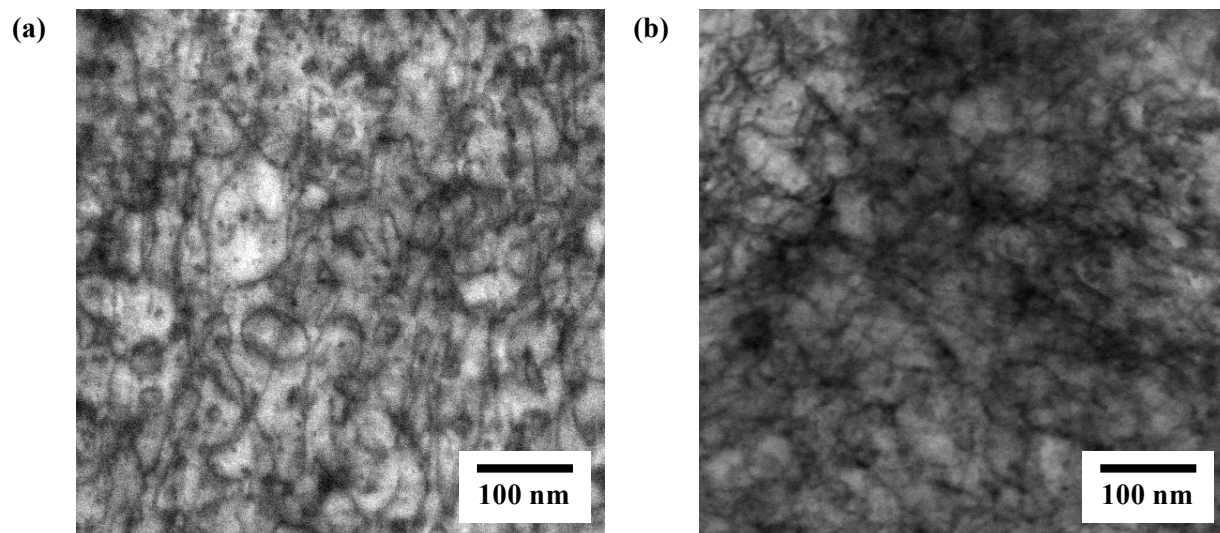
Figure 8: Dislocation structure in neutron irradiated C35M (1.8 dpa at 364°C) in a low-strain region (a) and high strain region (b) of the SS-2E tensile specimen. Imaged using on-[100] zone axis STEM bright field imaging.

4.   DISCUSSION

The observed dislocation loop and Cr-rich α' microstructure in the non-deformed but irradiated C35M specimen is consistent with previous reports on neutron irradiated FeCrAl alloys irradiated to similar conditions. Here, a higher density of $a/2 \langle 111 \rangle$ loops compared to $a\langle 100 \rangle$ which is consistent with the defect structures observed in a 12 wt.% Cr, 5 wt.% model FeCrAl alloy irradiated to 1.8 dpa at 382°C [4]. Given this, the C35M alloy showed a reduced size of the $a\langle 100 \rangle$ loops compared to the model alloy which could be due to the increased irradiation temperature and/or variances in compositions between the two. For other loop types and the α' precipitates, the sizes are within reasonable agreement when experimental counting and sizing error is taken into account. The observed volume fraction of α' is consistent with the Cr composition dependencies shown in previous reports on model FeCrAl alloys [4,14]. The lack of cavities in the defect structure continues to support the on-going observations that FeCrAl alloys have a strong resistance to swelling at irradiation doses below 25 dpa [4,23,24].

The observed ductile response is in agreement with previous studies completed on model FeCrAl alloys. For example, Figure 9 shows a preliminary deformation map for high-Cr ferritic alloys based on the map in Figure 1 and experimental observations on irradiated model FeCrAl alloys [5] and aged FeCr alloys [6]. The C35M specimen resides within the ductile regime for model alloys due to the lower-Cr content, low dose (1.8 dpa, ~548 hr) irradiation. Studies conducted by Park et al. [6] showed that brittle fracture of a 30 wt.% FeCrAl alloy can be attributed in part to twinning and hence an arbitrary boundary is shown for brittle (twinning) and ductile (cells+screws+channeling) regimes within Figure 9. The current STEM-based observations of irradiated C35M showed the formation of dislocation cells, dislocation pile-ups, and screw dislocations which supports the proposed regions within Figure 9.

The retained ductility and deformation mechanics observed in this work suggests within the temperature-dose regime studied that Generation II FeCrAl alloys are viable for use as ATF LWR cladding when only tensile properties and performance are a concern. It is anticipated that cladding tubes may have behavior similar to those observed here for sheet specimens, although factors such as texturing due to the cold/warm-drawing processes should be considered. Further work is needed to determine the applicability

of the presented results to those of commercially produced cladding or additional temperature-dose regimes.
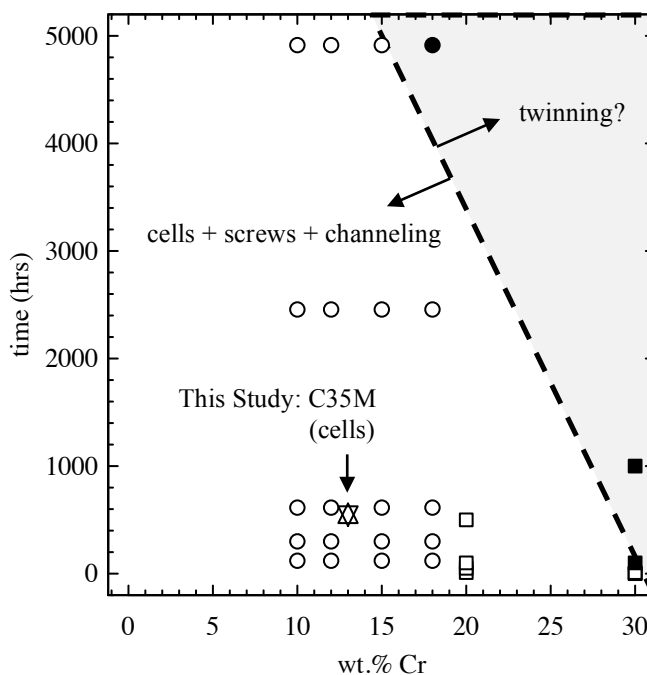
Figure 9: Preliminary deformation map of high-Cr ferritic alloys based on experimental observations. Open symbols are those tests which failed in a ductile manner, closed are those that failed in a brittle manner. Circles: irradiated Gen. I FeCrAl data [5], squares: aged model FeCr data [6], star: this study. Dpa converted to hours based on dpa rates.

5.   CONCLUSIONS

The deformation behavior and deformation microstructure of the neutron irradiated C35M Generation II FeCrAl alloy was observed using complementary testing and evaluation techniques. The observed ductile behavior can be attributed to the formation of dislocation cells and dislocation pileups within the deformed microstructure. Localized deformation in the manner of dislocation channeling and/or deformation-induced twinning was not observed. The observed results suggest that Generation II FeCrAl alloys retain ductility under low-dose, prototypical LWR irradiation conditions.

6.   ACKNOWLEDGEMENTS

7.   REFERENCES

[1]   K.A. Terrani, S.J. Zinkle, L.L. Snead, Advanced oxidation-resistant iron-based alloys for LWR fuel cladding, J. Nucl. Mater. 448 (2014) 420–435. doi:10.1016/j.jnucmat.2013.06.041.

[2]   B.A. Pint, K.A. Unocic, K.A. Terrani, The effect of steam on the high temperature oxidation

behavior of alumina-forming alloys, Mater. High Temp. 32 (2014) 28–35.

[3]   B.A. Pint, K.A. Terrani, M.P. Brady, T. Cheng, J.R. Keiser, High temperature oxidation of fuel cladding candidate materials in steam–hydrogen environments, J. Nucl. Mater. 440 (2013) 420–427. doi:10.1016/j.jnucmat.2013.05.047.

[4]   K.G. Field, X. Hu, K.C. Littrell, Y. Yamamoto, L.L. Snead, Radiation tolerance of neutron-irradiated model Fe-Cr-Al alloys, J. Nucl. Mater. 465 (2015) 746–755. doi:10.1016/j.jnucmat.2015.06.023.

[5]   K.G. Field, S.A. Briggs, K. Sridharan, R.H. Howard, Y. Yamamoto, Mechanical Properties of Neutron-Irradaited Model and Commercial FeCrAl Alloys, J. Nucl. Mater. 489 (2017) 118–128.

[6]   K.-H. Park, J.C. LaSalle, L.H. Schwartz, M. Kato, Mechanical properties of spinodally decomposed Fe-30 wt% Cr alloys: Yield strength and aging embrittlement, Acta Metall. 34 (1986) 1853–1865. doi:10.1016/0001-6160(86)90130-6.

[7]   A. Triki, F. Bley, Y. Brechet, F. Louchet, On the origin of hardening in aged FeCr alloys: relation between unmixing and mechanical properties, in: U. Messerschmidt, F. Appel, J. Heydenreich, V. Schmidt (Eds.), Electron Microsc. Plast. Fract. Res. Mater., Akademie-Verlag, Berlin, 1989: pp. 139–147.

[8]   K. Wang, Y. Dai, P. Spätig, Microstructure and fracture behavior of F82H steel under different irradiation and tensile test conditions, J. Nucl. Mater. 468 (2016) 246–254. doi:10.1016/j.jnucmat.2015.09.031.

[9]   Y. Yamamoto, B.A. Pint, K.A. Terrani, K.G. Field, Y. Yang, L.L. Snead, Development and property evaluation of nuclear grade wrought FeCrAl fuel cladding for light water reactors, J. Nucl. Mater. 467 (2015) 703–716. doi:10.1016/j.jnucmat.2015.10.019.

[10]   M.N. Gussev, R.H. Howard, K.A. Terrani, K.G. Field, Sub-size tensile specimen design for in-reactor irradiation and post-irradiation testing, Nucl. Eng. Des. 320 (2017) 298–308. doi:10.1016/j.nucengdes.2017.06.008.

[11]   A.A. Campbell, W.D. Porter, Y. Katoh, L.L. Snead, Method for analyzing passive silicon carbide thermometry with a continuous dilatometer to determine irradiation temperature, Nucl. Instruments Methods Phys. Res. Sect. B Beam Interact. with Mater. Atoms. 370 (2016) 49–58. doi:10.1016/j.nimb.2016.01.005.

[12]   K.G. Field, M.N. Gussev, R. Howard, First Annual Progress Report on Radiation Tolerance of Controlled Fusion Welds in High Temperature Oxidation Resistant FeCrAl Alloys, ORNL/TM-2015/770. (2015).

[13]   K.G. Field, M.N. Gussev, Y. Yamamoto, R. Howard, S. Briggs, Second Annual Progress Report on Radiation Tolerance of Controlled Fusion Welds in High Temperature Oxidation Resistant FeCrAl Alloys, ORNL/TM-2016/770. (2016). http://www.ntis.gov/help/ordermethods.aspx (accessed July 16, 2017).

[14]   S.A. Briggs, P.D. Edmondson, K.C. Littrell, Y. Yamamoto, R.H. Howard, C.R. Daily, K.A. Terrani, K. Sridharan, K.G. Field, A combined APT and SANS investigation of α′ phase precipitation in neutron-irradiated model FeCrAl alloys, Acta Mater. 129 (2017) 217–228. doi:10.1016/j.actamat.2017.02.077.

[15]   C. Heintze, F. Bergner, A. Ulbricht, H. Eckerlebe, The microstructure of neutron-irradiated Fe–Cr alloys: A small-angle neutron scattering study, J. Nucl. Mater. 409 (2011) 106–111. doi:10.1016/j.jnucmat.2010.09.010.

[16]   A. Ulbricht, C. Heintze, F. Bergner, H. Eckerlebe, SANS investigation of a neutron-irradiated Fe–9at%Cr alloy, J. Nucl. Mater. 407 (2010) 29–33. doi:10.1016/j.jnucmat.2010.07.005.

[17]   M.H. Mathon, Y. de Carlan, G. Geoffroy, X. Averty, A. Alamo, C.H. de Novion, A SANS investigation of the irradiation-enhanced α–α′ phases separation in 7–12 Cr martensitic steels, J. Nucl. Mater. 312 (2003) 236–248. doi:10.1016/s0022-3115(02)01630-6.

[18]   M.-H. Mathon, Y. De Carlan, X. Averty, A. Alamo, C.-H. De Novion, Small Angle Neutron Scattering Study of Irradiated Martensitic Steels: Relation Between Microstructural Evolution and Hardening, J. ASTM Int. 2 (2005). www.astm.org (accessed August 26, 2016).

[19]   Z. Száraz, G. Török, V. Kršjak, P. Hähner, SANS investigation of microstructure evolution in high chromium ODS steels after thermal ageing, J. Nucl. Mater. 435 (2013) 56–62. doi:10.1016/j.jnucmat.2012.12.016.

[20]   B. Yao, D.J. Edwards, R.J. Kurtz, TEM characterization of dislocation loops in irradiated bcc Fe-based steels, J. Nucl. Mater. 434 (2013) 402–410. doi:10.1016/j.jnucmat.2012.12.002.

[21]   K.G. Field, M.N. Gussev, Radiation Tolerance of Controlled Fusion Welds in high Temperature Oxidation Resistant FeCrAl Alloys, ORNL/TM-2017/379. (2017).

[22]   K.G. Field, S.A. Briggs, P.D. Edmondson, J.C. Haley, R.H. Howard, X. Hu, K.C. Littrell, C.M. Parish, Y. Yamamoto, Database on Performance of Neutron Irradiated FeCrAl Alloys, ORNL/TM-2016/335. (2016).

[23]   E.A. Little, D.A. Stow, Void-swelling in irons and ferritic steels: II. An experimental survey of materials irradiated in a fast reactor, J. Nucl. Mater. 87 (1979) 25–39.

[24]   K.G. Field, S.A. Briggs, X. Hu, Y. Yamamoto, R.H. Howard, K. Sridharan, Heterogeneous dislocation loop formation near grain boundaries in a neutron-irradiated commercial FeCrAl alloy, J. Nucl. Mater. 483 (2017) 54–61. doi:10.1016/j.jnucmat.2016.10.050.